SLAC-PUB-9210
September 2002
Revised

Neutron Energy and Time-of-flight Spectra Behind the Lateral Shield of a High Energy Electron Accelerator Beam Dump, Part II: Monte Carlo Simulations *

S. Roesler
CERN, CH-1211 Geneva 23, Switzerland
J. C. Liu, S. H. Rokni
Stanford Linear Accelerator Center, Stanford University, Stanford, California 94309
S. Taniguchi
Japan Synchrotron Radiation Research Institute, Koto 1-1-1, Mikazuki-cho, Sayo-gun, Hyogo, 679-5198, Japan

Abstract

Energy spectra of high-energy neutrons and neutron time-of-flight spectra were calculated for the setup of experiment T-454 performed with a NE213 liquid scintillator at the Final Focus Test Beam (FFTB) facility at the Stanford Linear Accelerator Center. The neutrons were created by the interaction a 28.7 GeV electron beam in the aluminum beam dump of the FFTB which is housed inside a thick steel and concrete shielding. In order to determine the attenuation length of high-energy neutrons additional concrete shielding of various thicknesses was placed outside the existing shielding. The calculations were performed using the FLUKA interaction and transport code. The energy and time-of-flight were recorded for the location of the detector allowing a detailed comparison with the experimental data. A generally good description of the data is achieved adding confidence to the use of FLUKA for the design of shielding for high-energy electron accelerators.

Submitted to Nuclear Instruments and Methods in Physics Research: Section A. Accelerators

*Work supported by Department of Energy contract DE-AC03-76SF00515

Neutron Energy and Time-of-flight Spectra Behind the Lateral Shield of a High Energy Electron Accelerator Beam Dump, Part II: Monte Carlo Simulations

S. Roesler, [a,*] J. C. Liu, [b] S. H. Rokni, [b] S. Taniguchi [c]

[a] *CERN, CH-1211 Geneva 23, Switzerland*

[b] *Stanford Linear Accelerator Center, MS. 48, 2575 Sand Hill Road, Menlo Park, California 94025, USA*

[c] *Japan Synchrotron Radiation Research Institute, Koto 1-1-1, Mikazuki-cho, Sayo-gun, Hyogo, 679-5198, Japan*

Abstract

Energy spectra of high-energy neutrons and neutron time-of-flight spectra were calculated for the setup of experiment T-454 performed with a NE213 liquid scintillator at the Final Focus Test Beam (FFTB) facility at the Stanford Linear Accelerator Center. The neutrons were created by the interaction a 28.7 GeV electron beam in the aluminum beam dump of the FFTB which is housed inside a thick steel and concrete shielding. In order to determine the attenuation length of high-energy neutrons additional concrete shielding of various thicknesses was placed outside the existing shielding. The calculations were performed using the FLUKA interaction and transport code. The energy and time-of-flight were recorded for the location of the detector allowing a detailed comparison with the experimental data. A generally good description of the data is achieved adding confidence to the use of FLUKA for the design of shielding for high-energy electron accelerators.

Key words: Electron accelerator, Neutron spectrum, Time-of-flight spectrum, Deep penetration, FLUKA

1 Introduction

The radiation environment outside lateral, thick shielding at high-energy electron accelerators, e.g., as can be found around beam dumps or collimators, is characterized by neutrons and photons of a wide energy range. Dose to personnel is dominated by the neutrons of which those with high energies ($E > 20$ MeV) contribute a significant fraction.

High-energy neutrons are produced in inelastic hadronic interactions of secondary (bremsstrahlung) photons in the beam line elements or dumps. Depending on the energy of the photon different models are commonly used to describe the interaction process. In the energy range between approximately 30 MeV and 200 MeV the process can be understood as a quasi-deuteron absorption of the photon followed by an intranuclear cascade and a de-excitation of the target nucleus. At energies between 200 MeV and a few GeV delta resonance production and decay, again accompanied by an intranuclear cascade and nuclear de-excitation, governs neutron production. At even higher energies the photon is assumed to fluctuate into a hadronic state (vector meson) which subsequently interacts hadronically, similarly to a pion.

* Corresponding author. Tel.: +41-22-7679891, Fax: +41-22-7675700, E-mail address: Stefan.Roesler@cern.ch

As a result of such interactions hadrons (neutrons, protons, pions) are emitted which may re-interact in the dump or beam line components. If emitted under a sufficiently large angle these secondary hadrons may also hit the lateral shielding where they are depleted in energy and attenuated in further particle cascades. Thus, the neutrons which are eventually emitted on the outer shield surface are of high generation in the “tree” of the electromagnetic and hadronic cascade. Any simulation attempting to predict the high-energy neutron spectra outside thick shields is therefore very sensitive to even small inaccuracies at each interaction or transport step as they may add up to sizeable uncertainties.

This fact underlines the importance of benchmarking calculations of high-energy neutron spectra with experimental data. Unfortunately, only very few experiments have performed high-energy neutron measurements outside thick shields at electron accelerators [1,2]. One of these measurements was performed by experiment T-454 outside the steel and concrete shield of the dump cavern of the Final Focus Test Beam (FFTB) at the Stanford Linear Accelerator Center (SLAC) at an electron beam energy of 28.7 GeV.

In this experiment high-energy neutron and time-of-flight (TOF) spectra were measured behind shielding of different thicknesses with a NE213 organic liquid scintillator. Details of the measurements and data analysis can be found in [2]. The present paper discusses the Monte Carlo (MC) simulations of the experiment performed with the FLUKA particle interaction and transport code [3,4].

2 The FLUKA Calculations

The calculations were carried out with the year 2000 version of the particle interaction and transport code FLUKA. The program has been used to simulate the electromagnetic and hadronic particle cascade in the FFTB dump and the surrounding shielding. In the following, details of the calculations are discussed which are of importance for the present study.

2.1 Description of the Geometry

The geometry is described in a right-handed orthogonal system with its origin centered on the front face of the FFTB dump, x pointing up, and z coinciding with the beam axis. Horizontal and vertical sections through the geometry are shown in Figs. 1 and 2.

The dump consists of an aluminum cylinder with a radius of 19 cm and a length of 145 cm followed by a 18 cm-long steel cylinder of the same radius. Any support structures of the dump were omitted in the FLUKA geometry. The center of the dump is at 37.12 cm above the concrete floor. A steel plate of a thickness of 15.24 cm is located directly above the dump.

The dump shielding consists of an inner steel and an outer concrete enclosure separated by an air gap. The lateral steel enclosure has a thickness of 83.82 cm (2 feet and 9 inches) and the lateral concrete enclosure of 182.88 cm (6 feet). For the experiment additional concrete shielding blocks were placed outside the southern, longitudinal side of the shield (i.e., in positive y-direction) allowing to measure the neutron spectra at three different concrete shield thicknesses: 274.32 cm (9 feet), 335.28 cm (11 feet), and 396.24 cm (13 feet). No measurements were taken with the default thickness of 182.88 cm in order to avoid pulse pile-up in the detector. Figs. 1 and 2 show the geometry for the 274.32 cm thick shield.

As the measurements were performed on the South side of the shield only the particle cascade in that direction was of interest in the simulation. Therefore, the outer part of the steel shield in the other directions was assumed to be "Blackhole" (see Figs. 1 and 2) – a pseudo-material in FLUKA terminating the particle cascade. Only an inner steel layer of about 20 cm was kept in order to correctly simulate particles scattered back into the dump cavern.

2.2 Materials and Simulation Parameters

The concrete shield was assumed to have a density of 2.35 g/cm^3 and the following chemical composition (the values in brackets give the corresponding mass fractions): oxygen (50.0%), silicon (20.0%), calcium (19.5%), aluminium (3.0%), carbon (3.0%), iron (1.4%), sodium (1.0%), potassium (1.0%), hydrogen (0.6%), and magnesium (0.5%). All steel shielding components including the back-end of the dump were assumed to consist of iron, nickel, and chromium with an atom relative content of 0.7, 0.2, and 0.1, respectively, and a density of 7.5 g/cm^3.

In order to obtain the neutron spectrum outside the shield over the whole energy range transport cutoffs were set to much lower energies (0.414 eV, i.e., all energies except thermal) than would have been required for the calculation of only the high-energy neutron spectrum. Photons and electrons were transported down to 100 keV and 1 MeV (kinetic energy), respectively, neutron interactions were simulated for all but thermal neutrons, and charged hadrons were followed until they are captured or decayed. For simplicity, the primary electron beam was assumed to be a pencil beam.

The use of several variance reduction (biasing) techniques was essential to obtain results with reasonable statistical significance. They included leading particle biasing at each electromagnetic interaction, biasing of the photon mean-free-path with respect to photonuclear interactions, and particle splitting during transport through the shield. To enable the latter the steel shield was split into layers (regions) of 10 cm thickness and the concrete shield into layers of 20 cm thickness. Each layer was assigned a different region-importance factor increasing in value toward the outside of the shield. The boundaries between the layers are shown in Figs. 1 and 2.

2.3 Calculated Quantities

Dedicated simulations were performed for the three different concrete shield thicknesses. In each case the following information on neutrons with an energy greater than 5 MeV and on photons of any energy emitted from the outer shield surface was recorded in a file for later analysis:

- Number of the primary electron.
- Generation of the particle. The generation of a particle increases with each sampled discrete interaction (electromagnetic or hadronic), i.e., the primary electron is generation "1," the generation of the photon after the first bremsstrahlung process would be "2," etc. Interactions which preserve

the incoming particle, e.g., elastic neutron scattering, do not increase the generation.

- Age (time-of-flight) of the particle with respect to the time at which the beam electron hits the dump.
- Weight of the particle.
- Kinetic energy.
- Coordinates (x and z) and direction cosines at the shield surface.

In order to restrict the analysis to approximately the area where the detectors were placed during the measurements and to still achieve reasonable statistical significance only those neutrons and photons were recorded which were emitted from a limited area. This area was on the shield surface and extended longitudinally from the front of the dump to the end of the dump cavern and vertically from about the beam axis to 150 cm above that axis. The area is marked in Figs. 1 and 2 by transverse lines through the concrete shield. In addition, one of the simulations also recorded neutrons and photons crossing the inner boundary of the southern part of the steel shield (y=152.4 cm, referred to as “source” below).

Furthermore, standard scoring capabilities of FLUKA were used to obtain the following quantities and spectra: the neutron energy spectrum outside the shield in the whole energy range including low-energy neutrons, the density of inelastic interactions with energies above 20 MeV (“stars”) in the dump and shielding components, and ambient dose equivalent rate throughout the whole geometry. The latter was calculated by folding particle fluence with energy-dependent conversion coefficients [5].

3 Results of the Simulations

3.1 Inelastic Interaction Density

The high-energy neutrons reaching the outside of the shield are produced in hadronic interactions of photons or in inelastic re-interactions of secondary hadrons inside the dump or in the shield. Fig. 3 shows the density profile of interactions at energies larger than 20 MeV for a horizontal slice through the geometry centered at the beam axis. The values are averaged in vertical (x-) direction over 40 cm. As expected, the interaction density is highest in the dump and in the steel shield. Only relatively few particles interact in the concrete shield (about two orders of magnitude less than in the steel shield).

The interaction density of photons and charged pions above 20 MeV is shown in Fig. 4. In the dump photons clearly dominate the total interaction density and contribute significantly to the interactions in the forward (transverse) steel shield. On the other hand, there are practically no high-energy photo-production interactions in the lateral shield. Similarly, photoproduced pions interact mainly in the dump and forward shield and only a few high-energy pions are emitted at larger angles and interact the steel shield.

Consequently, most of the high-energy inelastic interactions in the steel and concrete shields (see Fig. 3) are caused by neutrons with a minor contribution by protons. High energy neutrons which reach the outside of the shield are either produced directly in the dump or are secondary products of interacting neutrons.

3.2 Time-of-Flight Spectra

As mentioned above, neutrons with kinetic energies greater than 5 MeV and photons of all energies crossing the outer shield boundary were recorded in files. This allowed a detailed analysis of the distributions in the various variables by applying cutoffs, calculating correlations, or by the off-line folding with detector response functions. The comparison of calculated and measured TOF spectra is particularly important as it provides a benchmark of the Monte Carlo code which is independent from the uncertainties involved in the unfolding of the experimental count rates.

TOF spectra of neutrons and photons are shown for the different shield thicknesses in Fig. 5. All distributions are normalized per beam electron. Despite having recorded all neutrons down to 5 MeV, only those with energies larger than 20 MeV were included in the TOF spectra as this is the energy range of main interest for the experiment. The neutron spectra peak at about 37.3 ns, 41.6 ns, and 45.2 ns, respectively. The shift between the peaks of 3.6-4.3 ns reflects the increase in shield thickness of 60.96 cm. Using relativistic kinematics this shift corresponds to neutron energies between 120 MeV and 200 MeV.

The neutron and photon TOF spectra for the 274 cm thick shield are compared to each other in Fig. 6. As can be seen, photons and neutrons reach the outside of the shield at the same time. Taking into account that, in case of the 274 cm concrete shield, a photon would need only about 18 ns for the 549 cm distance between the center of the dump and the outside of the shield (i.e., less than half of the peak TOF) it can be concluded that these photons are secondary products of neutron interactions in the shield.

The calculated time-of-flight spectra can be directly compared to the count rates measured with the NE213 detector if they are folded with the energy efficiency function of the scintillator. This function is shown in Fig. 7a) for a light output threshold of 3 MeVee [2] corresponding to 6 MeV neutrons. As the detector responds to the number of neutrons the calculated *current* of neutrons above 5 MeV was used in the folding procedure. The resulting calculated count rates are compared to the measured count rates in Fig. 7b). The measured distribution has been shifted in TOF such that the measured and calculated peak-TOF agree with each other [2].

There is generally a good agreement in the center of the distributions. The measured tails of the distributions are underestimated in all cases which could be due to uncertainties in the response function at high energies (low TOF) and to uncertainties in the subtraction of the photon-induced signal. In addition, the measured TOF spectrum for the 274 cm shield shows a small peak at very low TOF which is not seen in the calculations.

3.3 Correlation between Time-of-Flight and Energy

From simple kinematic considerations it can be expected that there is a strong correlation between the energy of a neutron and its TOF. Fig. 8 shows the average energy of neutrons and photons outside the 274 cm and 396 cm thick concrete shields as function of the TOF.

The average neutron energy (Fig. 8a) is steeply decreasing with TOF. In addition, the average energy of the high-energy neutrons entering the steel shield ("source") is shown. Solid lines indicate the maximum possible neutron energy at the three boundaries assuming the neutron being emitted from the beam axis in a horizontal plane at 90 degrees. For the source-neutrons this line is to the left of the calculated dependency since most high-energy neutrons are emitted from the dump under smaller angles w.r.t. the beam axis, thus having a longer path and flight time to the steel shield. At the outer boundary of the concrete shield the situation is reversed. For pure geometrical reasons, neutrons reaching the scoring area at that boundary are caused by source neutrons emitted under larger angles. The 90 degree curve should therefore be a good approximation for the maximum energy. The calculated average energies are lower than the maximum value since the shield degrades the neutron energy. In addition, at large TOF the neutrons are produced in the concrete shield and have therefore much lower average energies.

The average photon energy (Fig. 8b) is also rapidly decreasing up to a TOF of about 40 ns (the maximum in the TOF spectrum) from where it stays approximately constant at around a few MeV, an energy typical for de-excitation photons after nuclear interactions in concrete.

The inverse correlation, i.e., the average TOF as function of energy is shown in Fig. 9. The top two solid lines in Fig. 9a) indicate the minimum TOF required for a neutron to reach the outside boundary of the respective concrete shield if it was emitted from the beam axis in a horizontal plane at 90 degree. At high energy ($E > 200$ MeV) the actual TOF is somewhat larger since the neutron path is longer due to smaller emission angles and scattering. At lower energies neutrons are secondary products of high energy neutron interactions in the shield and therefore reach the outside shield boundary earlier than as if they started their path with the same energy from the beam axis. The bottom solid line represents the minimum TOF for a neutron to reach the inner steel shield boundary, again assuming a 90 degree emission angle. The actual average TOF (symbols labelled “source”) is clearly larger because of the smaller emission angle and therefore larger flight paths. It is well fitted with an average TOF curve based on a 45 degrees emission angle (second solid line from the bottom).

As expected, high energy photons ($E > 20$ MeV) produced in neutron interactions in the shield arrive at the outer shield boundary earlier than neutrons of the same energy. This is shown in Fig. 9b) for the 274 cm concrete shield. Photons of lower energies accompany low-energy neutron interactions and therefore reach the outer shield boundary at larger TOF.

3.4 Average Particle Generation

As mentioned above, FLUKA keeps track of the particle generation in the tree of the cascade. Fig. 10a) shows this generation as function of the TOF for neutrons and Fig. 10b) for photons, respectively. Up to about 60 ns the average generation rises as the average energy decreases (c.f. Fig. 8). At larger TOF it stays approximately constant due to attenuation and possibly also due to effects of the 5 MeV threshold in recording the neutrons. Most of the increase in generation is caused in the strong electromagnetic cascade of the primary electron in the dump. The average generation of the neutrons at the inner steel boundary (symbols labelled “source” in Fig. 10a) is already relatively high and almost comparable to the one of the neutrons at the outside of the shield.

Photons, being secondary products of neutron interactions, show a similar dependence of generation on TOF as the neutrons up to a few hundred nanoseconds (Fig. 10b). At higher TOF the average generation is increasing rapidly as these photons are produced in low energy neutron interactions.

3.5 Energy Spectra

Energy spectra of neutrons and photons outside the shield are shown for the three concrete shield thicknesses in Fig. 11. As mentioned above, neutrons were scored in the whole energy range (including low energy neutrons) with standard scoring capabilities of FLUKA. The spectra are presented in units of lethargy, i.e. differential fluence $d\Phi/dE$ multiplied by energy E. The spectra are typical equilibrium spectra with a shape which is independent of the shield thickness. The area under the spectra corresponds to the number of particles indicating a significant contribution of high-energy neutrons (Fig. 11a).

The calculated high-energy neutron spectra are compared to the spectra measured with the NE213 organic liquid scintillator [2] in Fig. 12. Here, symbols represent the experimental data and histograms the FLUKA results. Except for very high energies ($E > 200$ MeV) there is generally a good agreement between measured and calculated spectra. The discrepancy at high energies is due to statistical uncertainties in the experimental data and uncertainties in the response function of the scintillator at these energies [2]. For the smallest thickness (274 cm) the calculated spectrum overestimates the measured one in the energy range between 10 MeV and 40 MeV. This is likely to be caused by an insufficient correction of the experimental data for pile-up events in the detector [2].

3.6 Dose Attenuation

As mentioned above, ambient dose equivalent rate was calculated by folding particle fluence with energy-dependent conversion coefficients [5]. Fig. 13 shows the dose rate from neutrons and photons for a horizontal slice through the geometry centered at the beam axis for the 274 cm concrete shield. The values are averaged in vertical (x-) direction over 40 cm. It should again be mentioned that thermal neutrons were not simulated. Therefore, the dose rates do neither include dose from thermal neutrons nor dose due to photons from thermal neutron capture. The figure clearly shows that the dose rate in- and outside the shield is dominated by neutrons.

Table 1 gives the ambient dose equivalent rate obtained by folding the measured and calculated neutron energy spectra (Figs. 11 and 12) with the conversion coefficients and by integrating them over energy. All values are normalized to a beam power of 1 kW. The integration of the measured spectra is limited to energies larger than 20 MeV to be able to compare them directly to the FLUKA results for high-energy neutrons (third column). There is generally a good agreement between the two values within about 15%. The contribution of high-energy neutrons to the total dose rate (ratio of the last two columns in Table 1) is independent of the shield thickness and about 57%. The attenuation coefficient for the high energy neutron dose in concrete obtained from the three calculated values is 116 g/cm^2.

Similarly, the photon dose rate can be calculated by folding the spectra of Fig. 11b) with energy dependent conversion coefficients. The resulting values are 10.4, 2.3, and 0.54 nSv/h/kW for the three shield thicknesses, respectively.

4 Summary and Conclusions

Energy and time-of-flight spectra of high-energy neutrons and of photons outside the dump shield of the Final Focus Test Beam at SLAC were calculated with the FLUKA Monte Carlo code. The aim of this study was to benchmark FLUKA with experimental data obtained with a NE213 organic liquid scintillator.

The aluminum beam dump as well as the steel and concrete shielding was simulated in detail. According to the experimental setup calculations were performed for three different thicknesses of the concrete shield between 274 cm and 396 cm. High energy neutrons and photons crossing the outer boundary of the concrete shield were recorded in files for later analysis. In addition, the density of inelastic interactions and ambient dose equivalent rate were scored for a horizontal slice through the center of the geometry.

High energy neutrons are created in hadronic interactions of photons and secondary hadrons in the dump and in interactions of neutrons and protons in the lateral shielding. There are practically no high-energy photoproduction interactions in the shielding. Photons reaching the outside of the shield are mainly produced in interactions of neutrons in the shield. The steel and concrete shield absorbs almost all photons produced in the dump.

The TOF spectra of neutrons and photons show a broad peak at about $35 - 50$ ns. There is generally a good agreement between calculated and measured TOF spectra except for the tails of the distributions. The comparison of the TOF spectra is particularly important as it provides a benchmark of the Monte Carlo code which is independent from the uncertainties involved in the un-folding of the experimental count rates. Various correlations between the energy and the TOF as well as between the generation of a particle and its TOF were studied confirming the origin of the components contributing to the TOF spectra.

Furthermore, energy spectra of neutrons (at all energies) and photons outside the shield were calculated and high-energy neutron spectra were compared to experimental data. The calculated spectra generally agree with the measured spectra within a factor of two. The discrepancies are caused by uncertainties in the response function of the NE213 detector at high energies, by uncertainties in the correction of the experimental data for pile-up events, and by statistical uncertainties of the measurement.

Finally, ambient dose equivalent rate was calculated by folding neutron and photon fluence with energy-dependent conversion factors. The dose outside the shield is mainly caused by neutrons of which those above 20 MeV contribute about 57%. Dose rates were also derived from the measured spectra by folding with the conversion factors. As observed for the energy spectra, a generally good agreement is obtained.

Acknowledgments

The authors are grateful to Alberto Fassò, Alfredo Ferrari, Kenneth R. Kase, and Takashi Nakamura for many stimulating discussions. This work was supported by the Department of Energy under contract DE-AC03-76SF00515.

References

[1] V. Vylet, J. C. Liu, S. H. Rokni, and L.-X. Thai, Radiat. Prot. Dosim. 70 (1997) 425.

[2] S. Taniguchi, et al., Neutron Energy and Time-of-flight Spectra Behind the Lateral Shield of a High Energy Electron Accelerator Beam Dump, Part I: Measurements, in preparation.

[3] A. Fassò, A. Ferrari, and P. R. Sala, Electron-photon transport in FLUKA: status, in: A. Kling, et al. (Eds.), Proceedings of the International Conference on Advanced Monte Carlo for Radiation Physics, Particle Transport Simulation and Applications, Monte Carlo 2000, Lisbon, Portugal, Oct. 2000, Springer-Verlag Berlin, Heidelberg, pp. 159-164.

[4] A. Fassò, A. Ferrari, J. Ranft, and P. R. Sala, FLUKA: Status and Prospective for Hadronic Applications, in: A. Kling, et al. (Eds.), Proceedings of the International Conference on Advanced Monte Carlo for Radiation Physics, Particle Transport Simulation and Applications, Monte Carlo 2000, Lisbon, Portugal, Oct. 2000, Springer-Verlag Berlin, Heidelberg, pp. 955-960.

[5] M. Pelliccioni, Radiat. Prot. Dosim. 88 (2000) 279.

Table Captions

Table 1. Neutron ambient dose equivalent rate outside the FFTB dump shield for different concrete shield thicknesses. Experimental values are compared to FLUKA predictions for the high-energy neutron dose rate. In addition, the calculated total neutron dose rate is given.

Figure Captions

Fig. 1. Horizontal section through the geometry used in the simulations. The beam axis runs vertically through the center of the aluminum dump. The origin of the coordinate frame is at the impact point of the beam on the dump. The beam pipe through the upstream part of the shield (bottom part in the figure) was omitted in the simulations.

Fig. 2. Vertical section through the geometry used in the simulations (z = 100 cm).

Fig. 3. Total density of inelastic interactions ("stars") at energies greater than 20 MeV. The figure shows a horizontal section through the dump cavern and the lateral shield at the height of the beam axis.

Fig. 4. As in Fig. 3, here the hadronic interaction density of photons (a) and of charged pions (b).

Fig. 5 Time-of-flight spectra of neutrons with energies greater than 20 MeV (a) and photons (b) behind different concrete shield thicknesses.

Fig. 6. Comparison of time-of-flight spectra of neutrons and photons behind a concrete shield thickness of 274 cm.

Fig. 7. a) Efficiency of the NE213 detector for a light output threshold of 3 MeVee. b) The calculated time-of-flight spectra for the different shield thicknesses (from the top to the bottom: 274 cm, 335 cm, and 396 cm) obtained by folding the current of neutrons crossing the outer shield boundary with the detector efficiency function (histograms) are compared to experimental data (points) [2].

Fig. 8. Average energy of neutrons (a) and photons (b) as function of time-of-flight behind concrete shield thicknesses of 274 cm and 396 cm (symbols). In addition, the average energy of neutrons at the inner boundary of the steel shield ("source") is shown. See text for a discussion of the solid lines.

Fig. 9. Average time-of-flight of neutrons (a) as function of energy behind concrete shield thicknesses of 274 cm and 396 cm and at the inner boundary of the steel shield (symbols). See text for an explanation of the solid lines. Figure b) shows a comparison of the average time-of-flight of neutrons and photons behind a concrete shield of 274 cm as function of energy.

Fig. 10. Average generation of neutrons (a) and of photons (b) as function of time-of-flight behind concrete shield thicknesses of 274 cm and 396 cm. For neutrons the average generation is given also for the inner boundary of the steel shield.

Fig. 11. Energy spectra of neutrons (a) and photons (b) behind concrete shield thicknesses of 274 cm, 335 cm, and 396 cm.

Fig. 12. Energy spectra of high-energy neutrons behind concrete shield thicknesses of 274 cm, 335 cm, and 396 cm. Calculated spectra are shown as histogram and measured spectra [2] as symbols.

Fig. 13. Neutron (a) and photon ambient dose equivalent rate (b) shown for a horizontal section through the dump cavern and the lateral shield (steel and 274 cm of concrete) at the height of the beam axis.

Table 1

Thickness (cm)	Experiment ($E > 20$ MeV) (μSv/h/kW)	FLUKA ($E > 20$ MeV) (μSv/h/kW)	FLUKA (all energies) (μSv/h/kW)
274	0.64	0.72	1.29
335	0.19	0.18	0.32
396	0.043	0.041	0.070

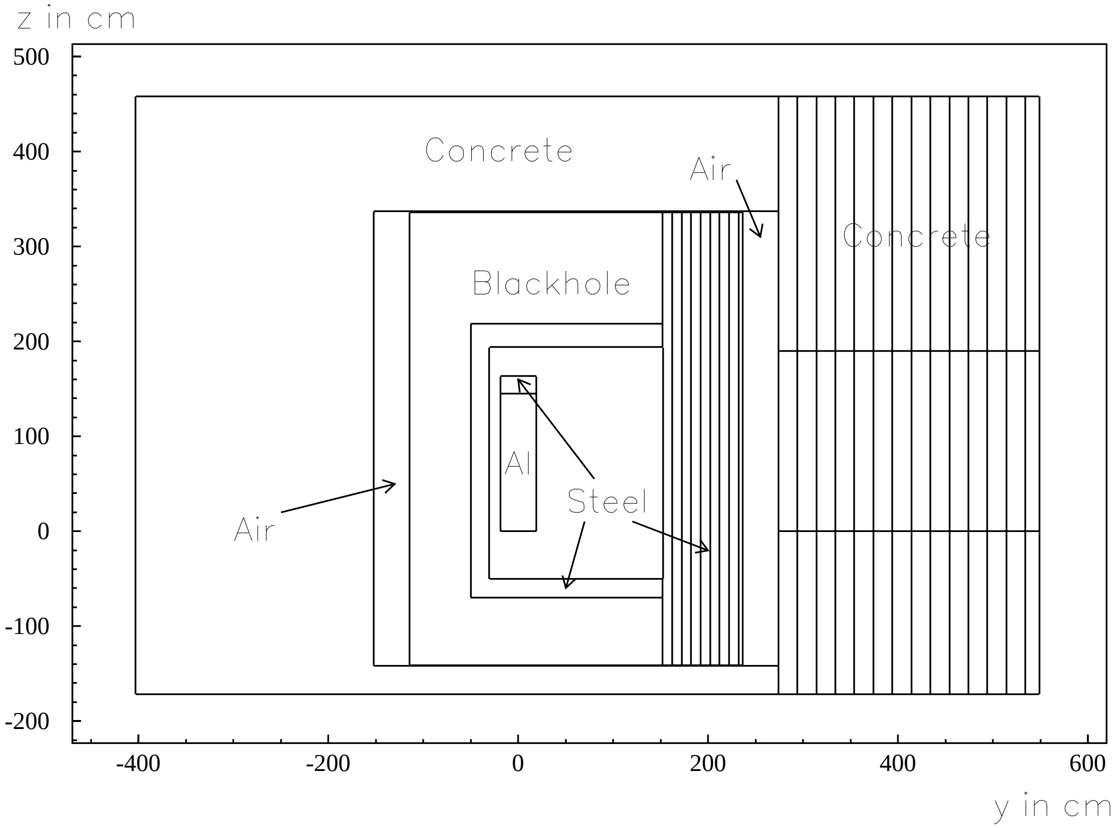
z in cm
500
400
300
200
100
0
-100
-200
-400
-200
0
200
400
600
y in cm
Concrete
Air
Concrete
Blackhole
Al
Air
Steel

Fig. 1.

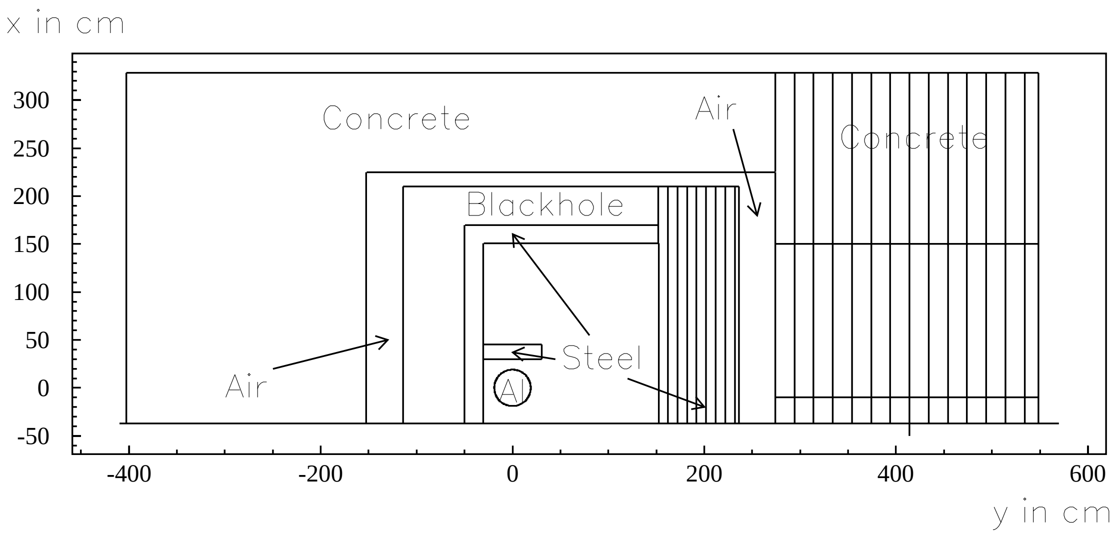

Fig. 2.

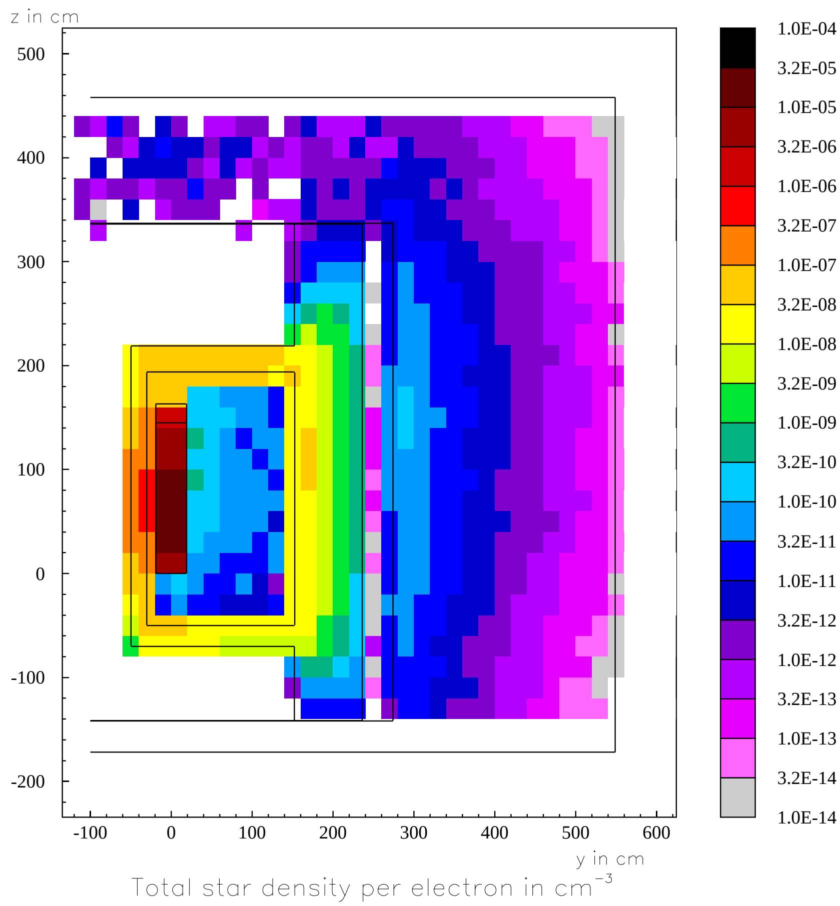
z in cm
500
400
300
200
100
0
-100
-200
-100
0
100
200
300
400
500
600
y in cm
Total star density per electron in cm^{-3}
1.0E-04
3.2E-05
1.0E-05
3.2E-06
1.0E-06
3.2E-07
1.0E-07
3.2E-08
1.0E-08
3.2E-09
1.0E-09
3.2E-10
1.0E-10
3.2E-11
1.0E-11
3.2E-12
1.0E-12
3.2E-13
1.0E-13
3.2E-14
1.0E-14

Fig. 3.

a)

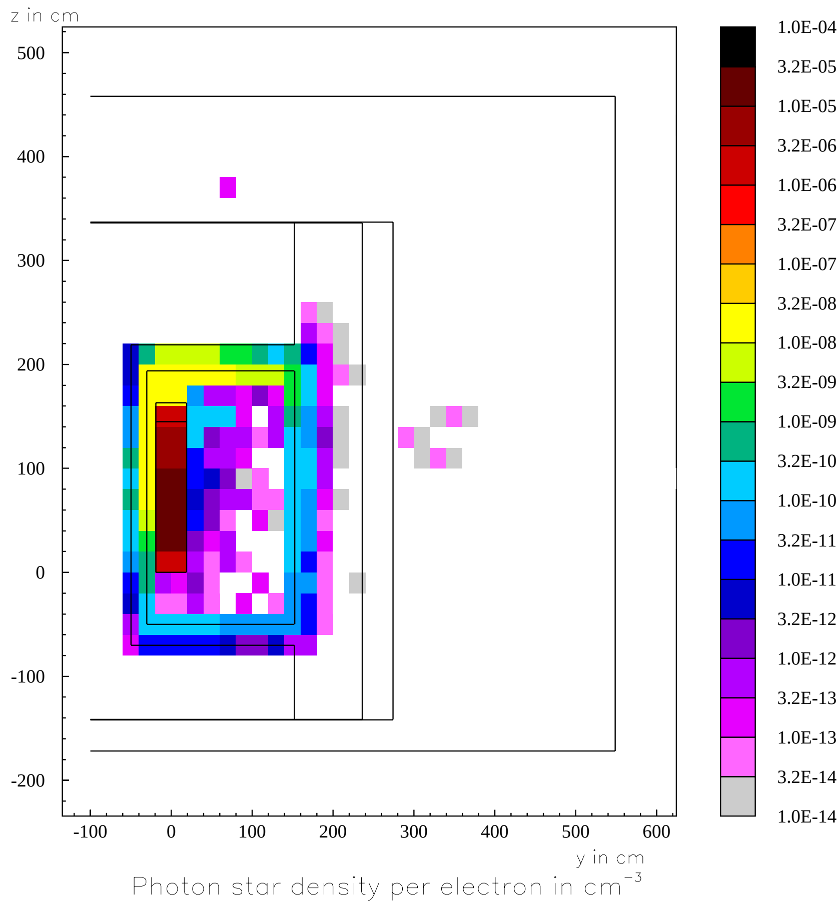

z in cm
500
400
300
200
100
0
-100
-200
-100
0
100
200
300
400
500
600
y in cm
1.0E-04
3.2E-05
1.0E-05
3.2E-06
1.0E-06
3.2E-07
1.0E-07
3.2E-08
1.0E-08
3.2E-09
1.0E-09
3.2E-10
1.0E-10
3.2E-11
1.0E-11
3.2E-12
1.0E-12
3.2E-13
1.0E-13
3.2E-14
1.0E-14
Photon star density per electron in cm^{-3}

b)

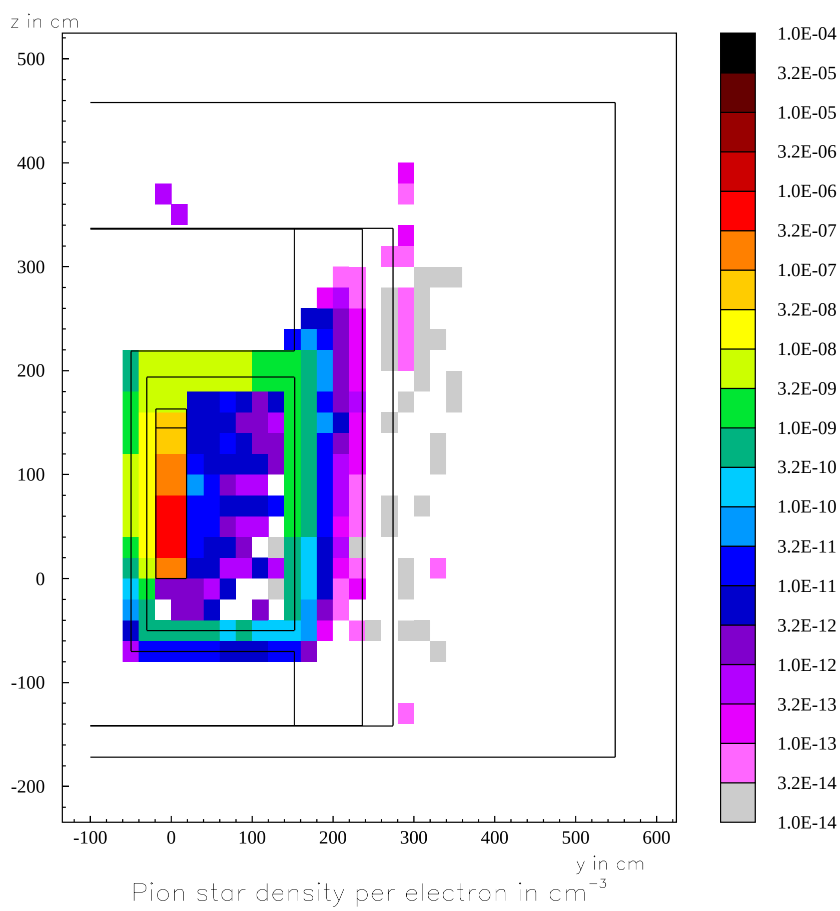

z in cm
500
400
300
200
100
0
-100
-200
-100
0
100
200
300
400
500
600
y in cm
1.0E-04
3.2E-05
1.0E-05
3.2E-06
1.0E-06
3.2E-07
1.0E-07
3.2E-08
1.0E-08
3.2E-09
1.0E-09
3.2E-10
1.0E-10
3.2E-11
1.0E-11
3.2E-12
1.0E-12
3.2E-13
1.0E-13
3.2E-14
1.0E-14
Pion star density per electron in cm^{-3}

Fig. 4.

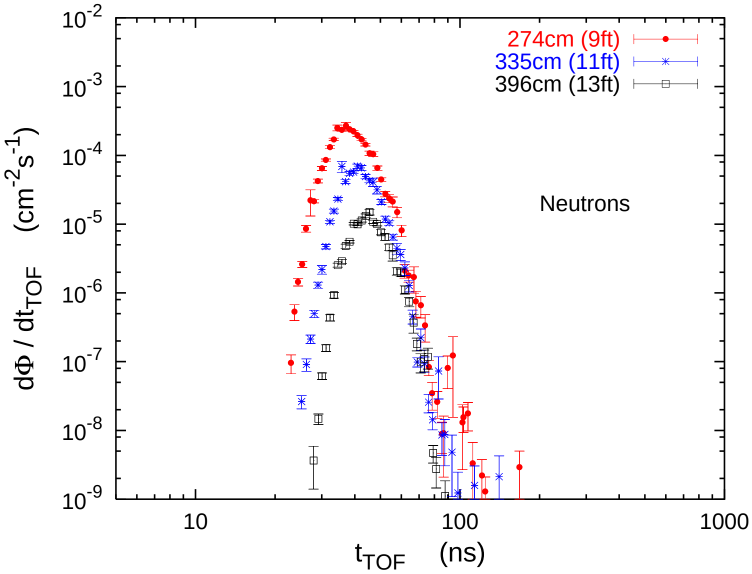

274cm (9ft)
335cm (11ft)
396cm (13ft)
Neutrons
dΦ / dt_TOF (cm^-2 s^-1)
t_TOF (ns)

a)

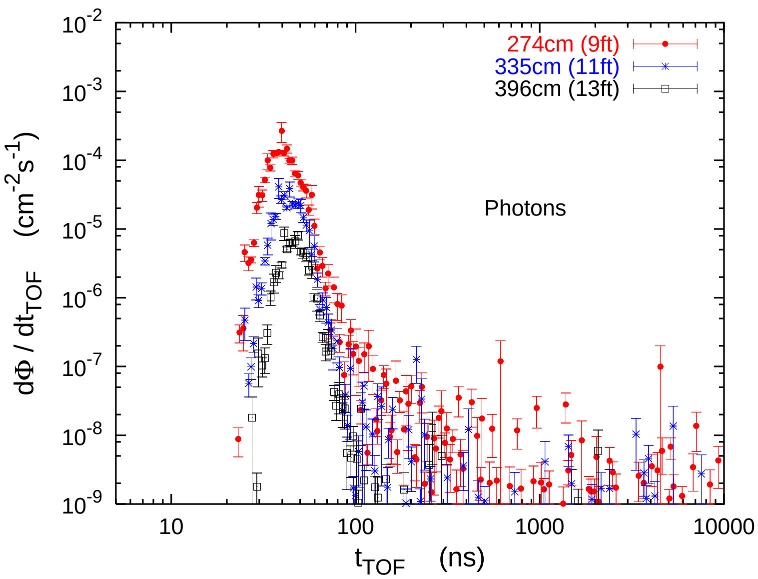

274cm (9ft)
335cm (11ft)
396cm (13ft)
Photons
dΦ / dt_TOF (cm^-2 s^-1)
t_TOF (ns)

b)

Fig. 5.

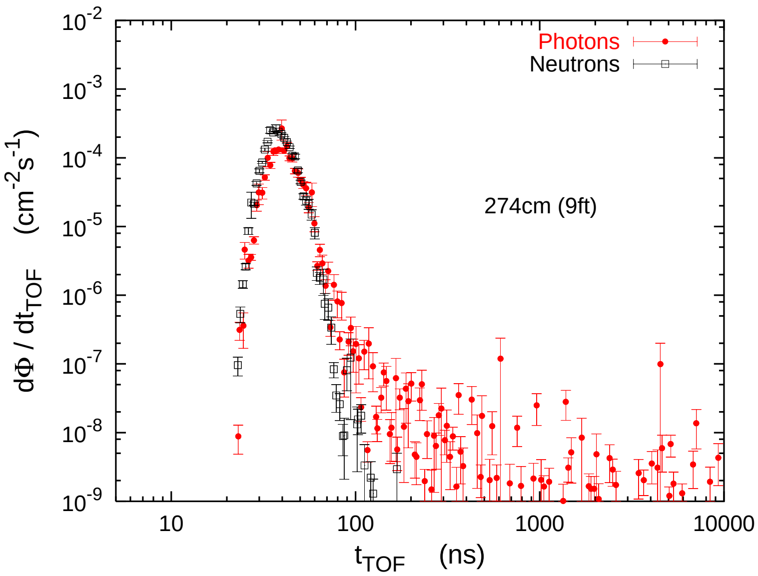

Photons
Neutrons
274cm (9ft)
dΦ / dt_TOF (cm^-2 s^-1)
t_TOF (ns)
10^-2
10^-3
10^-4
10^-5
10^-6
10^-7
10^-8
10^-9
10
100
1000
10000

Fig. 6.

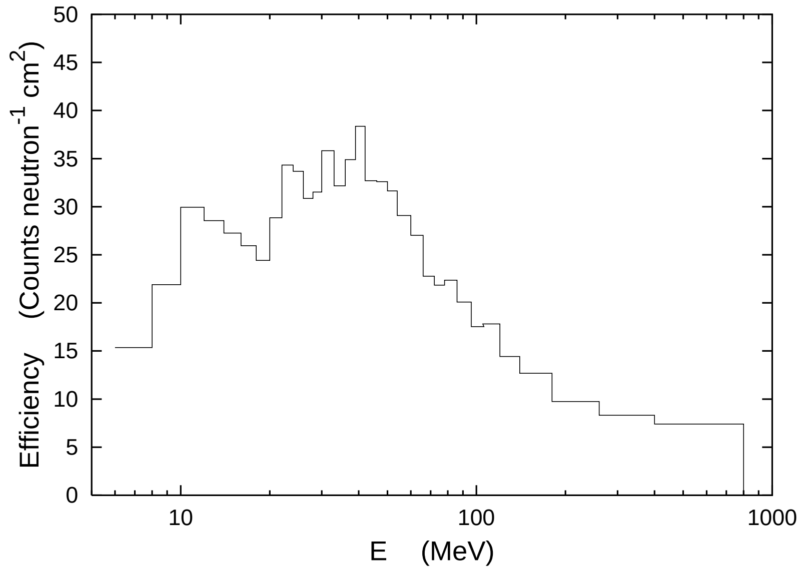

Efficiency (Counts neutron^{-1} cm^2)
E (MeV)

a)

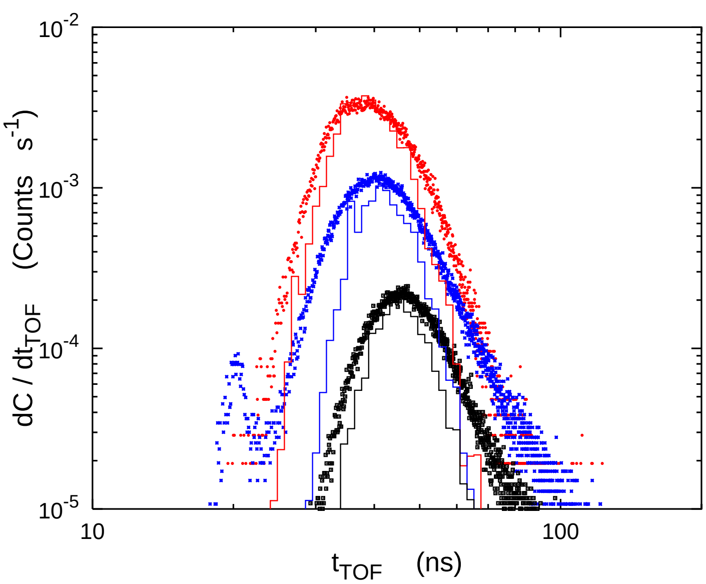

dC / dt$_{TOF}$ (Counts s^{-1})
t$_{TOF}$ (ns)

b)

Fig. 7.

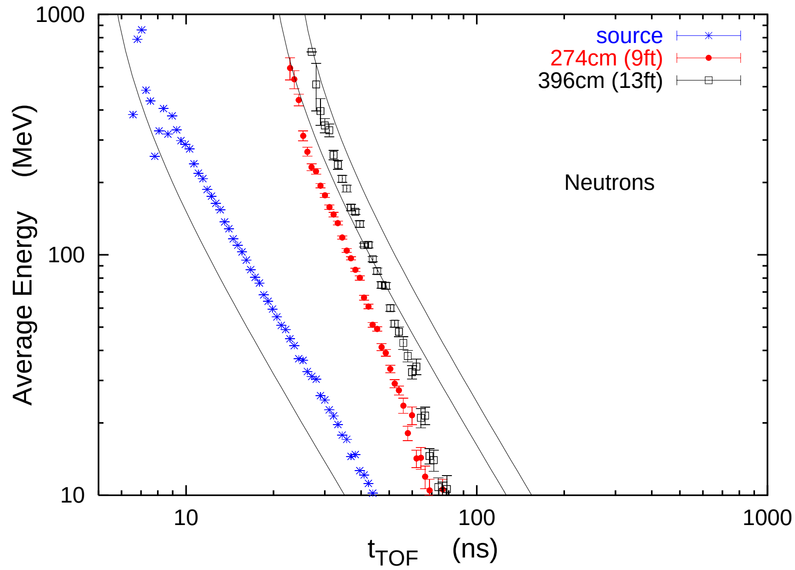

source
274cm (9ft)
396cm (13ft)
Neutrons
Average Energy (MeV)
t_{TOF} (ns)

a)

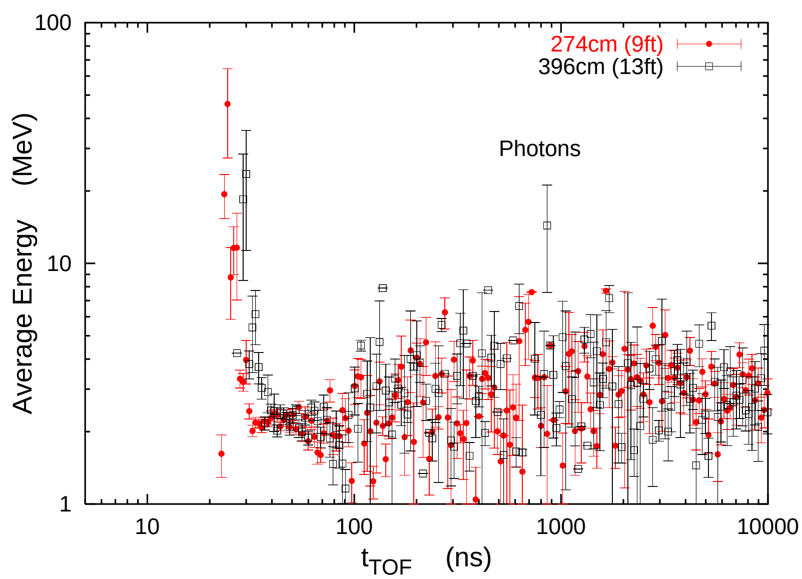

274cm (9ft)
396cm (13ft)
Photons
Average Energy (MeV)
t_{TOF} (ns)

b)

Fig. 8.

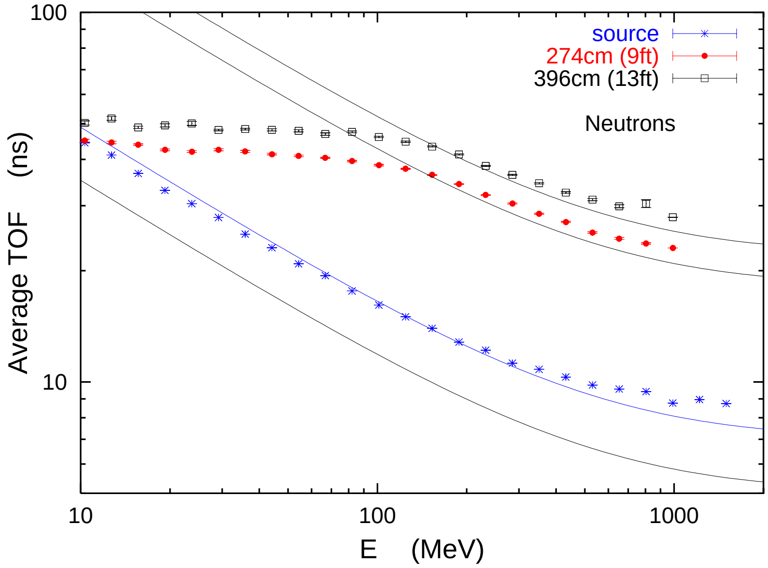

100
10
10
100
1000
E (MeV)
Average TOF (ns)
source
274cm (9ft)
396cm (13ft)
Neutrons

a)

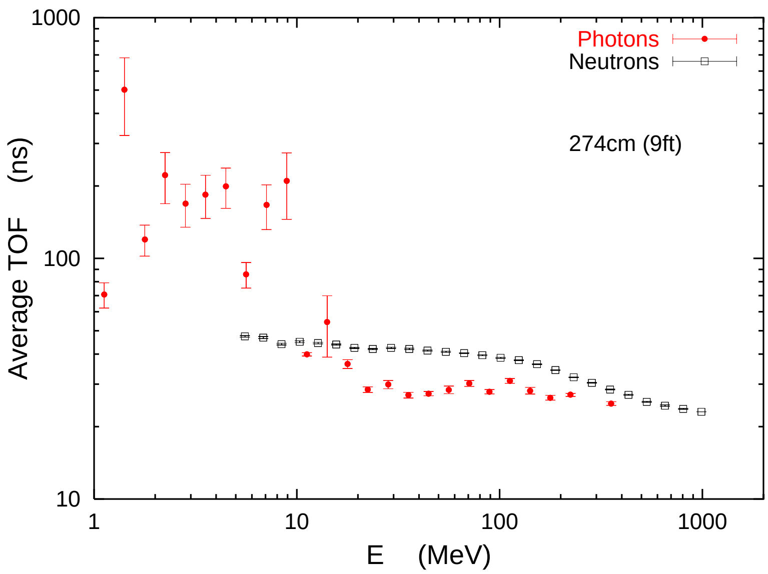

1000
100
10
1
10
100
1000
E (MeV)
Average TOF (ns)
Photons
Neutrons
274cm (9ft)

b)

Fig. 9.

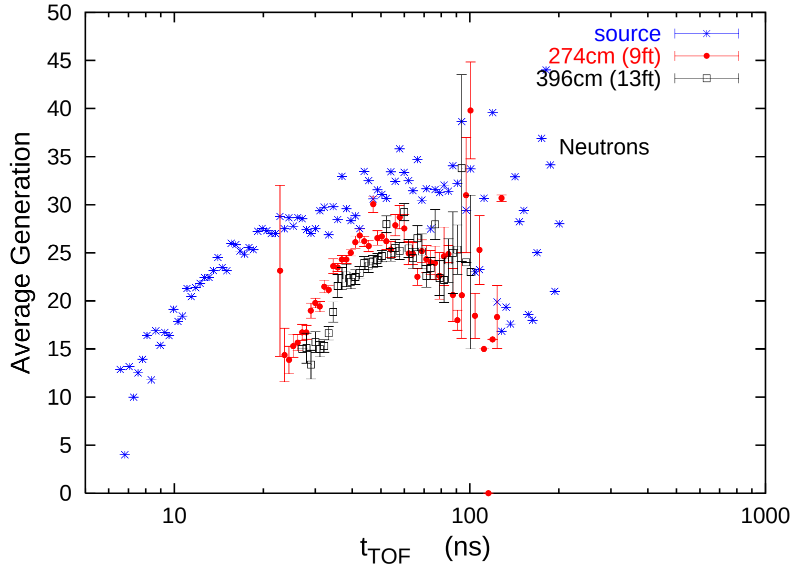

source
274cm (9ft)
396cm (13ft)
Neutrons
Average Generation
t_{TOF} (ns)

a)

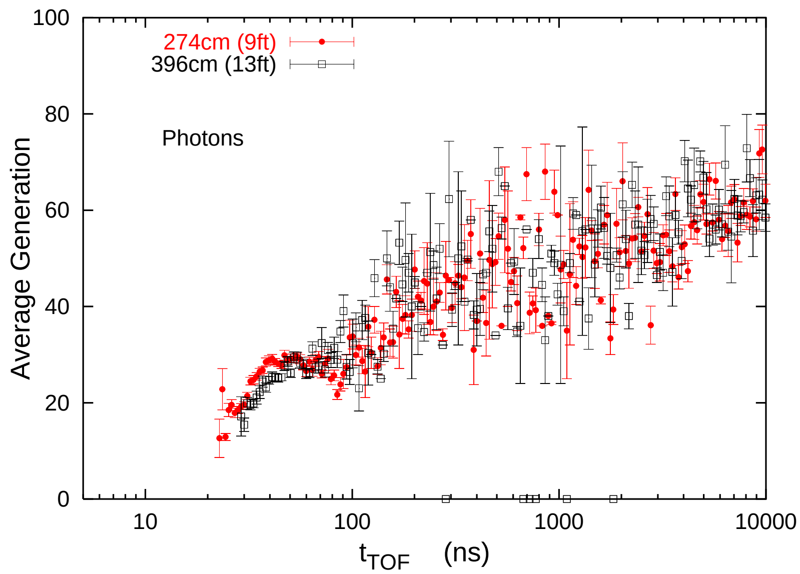

274cm (9ft)
396cm (13ft)
Photons
Average Generation
t_{TOF} (ns)

b)

Fig. 10.

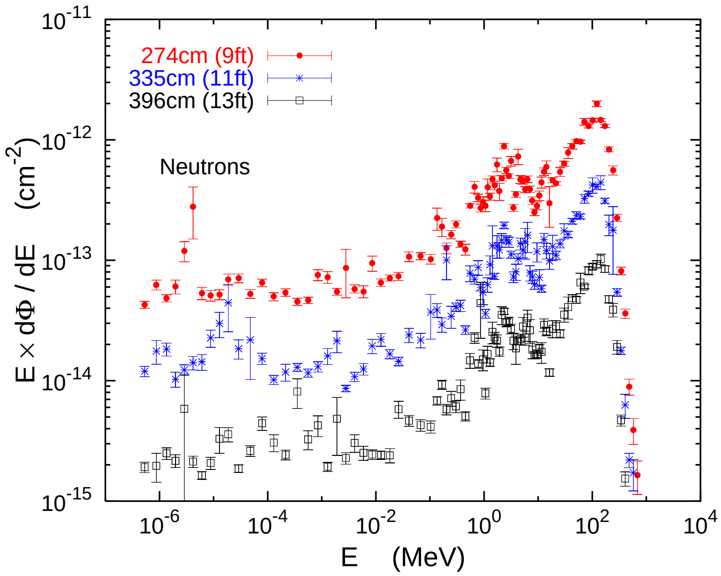
274cm (9ft)
335cm (11ft)
396cm (13ft)
Neutrons
E × dΦ / dE (cm^{-2})
E (MeV)

a)

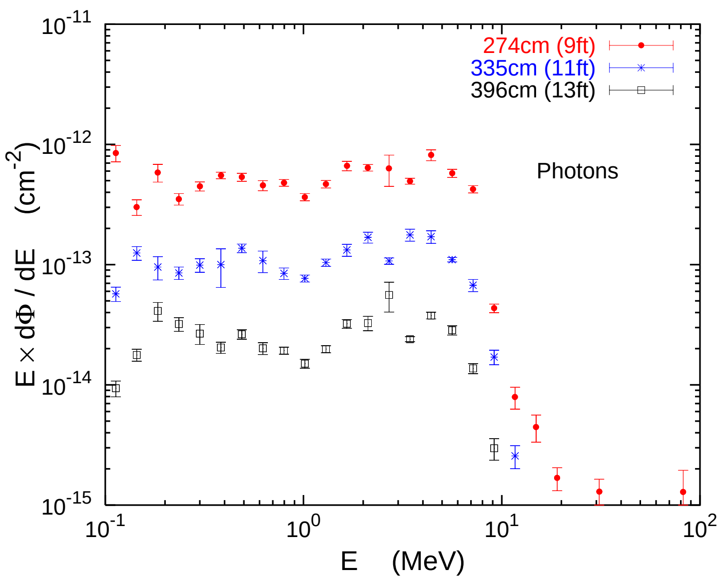
274cm (9ft)
335cm (11ft)
396cm (13ft)
Photons
E × dΦ / dE (cm^{-2})
E (MeV)

b)

Fig. 11.

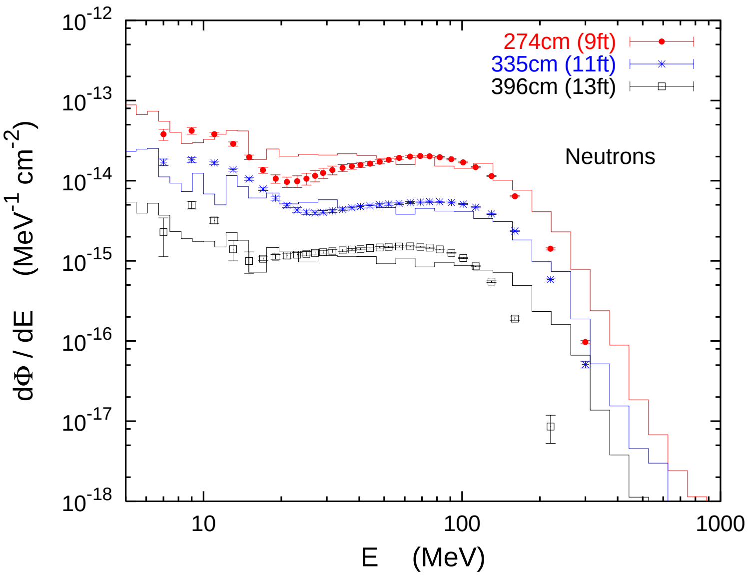

Fig. 12.

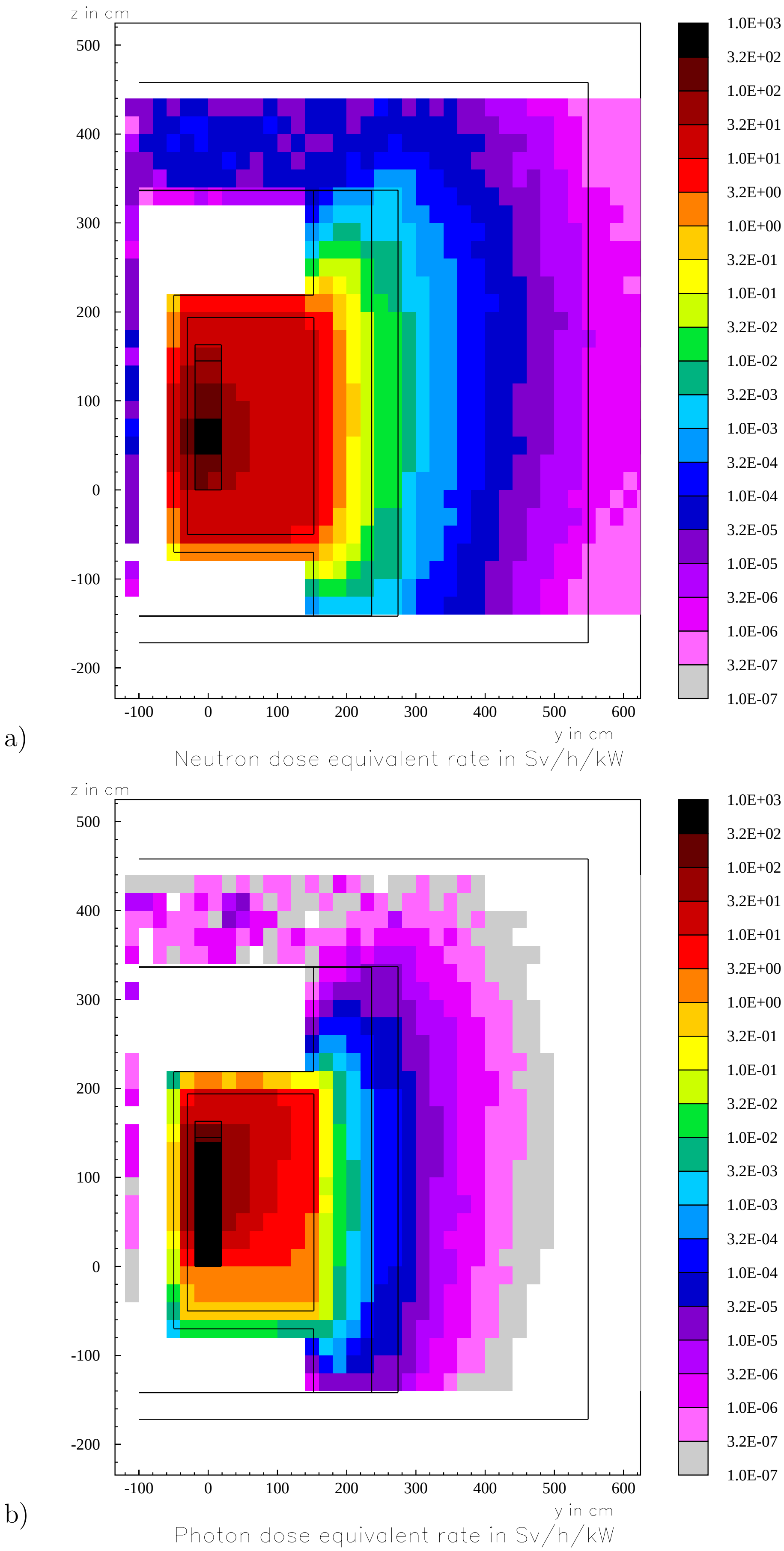
a)
z in cm
500
400
300
200
100
0
-100
-200
-100
0
100
200
300
400
500
600
y in cm
Neutron dose equivalent rate in Sv/h/kW
1.0E+03
3.2E+02
1.0E+02
3.2E+01
1.0E+01
3.2E+00
1.0E+00
3.2E-01
1.0E-01
3.2E-02
1.0E-02
3.2E-03
1.0E-03
3.2E-04
1.0E-04
3.2E-05
1.0E-05
3.2E-06
1.0E-06
3.2E-07
1.0E-07
b)
z in cm
500
400
300
200
100
0
-100
-200
-100
0
100
200
300
400
500
600
y in cm
Photon dose equivalent rate in Sv/h/kW
1.0E+03
3.2E+02
1.0E+02
3.2E+01
1.0E+01
3.2E+00
1.0E+00
3.2E-01
1.0E-01
3.2E-02
1.0E-02
3.2E-03
1.0E-03
3.2E-04
1.0E-04
3.2E-05
1.0E-05
3.2E-06
1.0E-06
3.2E-07
1.0E-07

Fig. 13.